Cell Reports, Volume *42*

Supplemental information

Structural insights into anion selectivity and activation mechanism of LRRC8 volume-regulated anion channels

Heng Liu, Maya M. Polovitskaya, Linlin Yang, Meiling Li, Hongyue Li, Zhen Han, Jianguo Wu, Qiansen Zhang, Thomas J. Jentsch, and Jun Liao

Figure S1

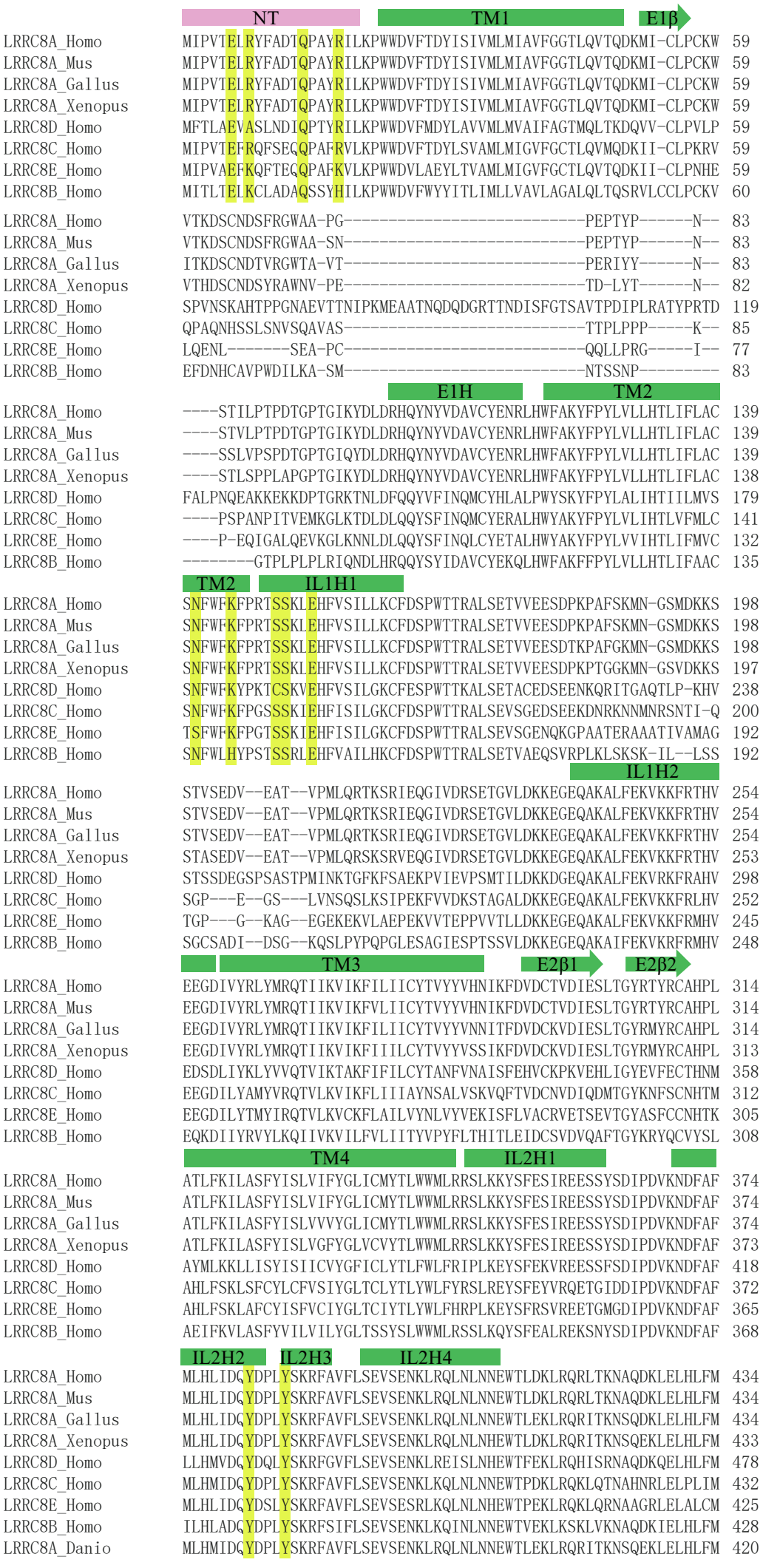
NT
TM1
E1β
LRRC8A_Homo MIPVTELRYFADTQPAYRILKPWWDVFTDYISIVMLMIAVFGGTLQVTQDKMI-CLPCKW 59
LRRC8A_Mus MIPVTELRYFADTQPAYRILKPWWDVFTDYISIVMLMIAVFGGTLQVTQDKMI-CLPCKW 59
LRRC8A_Gallus MIPVTELRYFADTQPAYRILKPWWDVFTDYISIVMLMIAVFGGTLQVTQDKMI-CLPCKW 59
LRRC8A_Xenopus MIPVTELRYFADTQPAYRILKPWWDVFTDYISIVMLMIAVFGGTLQVTQDKMI-CLPCKW 59
LRRC8D_Homo MFTLAEVASLNDIQPTYRILKPWWDVFMDYLAVVMLMVAIFAGTMQLTKDQVV-CLPVLP 59
LRRC8C_Homo MIPVTEFRQFSEQQPAFRVLKPWWDVFTDYLSVAMLMIGVFGCTLQVMQDKII-CLPKRV 59
LRRC8E_Homo MIPVAEFKQFTEQQPAFKVLKPWWDVLAEYLTVAMLMIGVFGCTLQVTQDKII-CLPNHE 59
LRRC8B_Homo MITLTELKCLADAQSSYHILKPWWDVFWYYITLIMLLVAVLAGALQLTQSRVLCCLPCKV 60
LRRC8A_Homo VTKDSCNDSFRGWAA-PG----------PEPTYP------N-- 83
LRRC8A_Mus VTKDSCNDSFRGWAA-SN----------PEPTYP------N-- 83
LRRC8A_Gallus ITKDSCNDTVRGWTA-VT----------PERIYY------N-- 83
LRRC8A_Xenopus VTHDSCNDSYRAWNV-PE----------TD-LYT------N-- 82
LRRC8D_Homo SPVNSKAHTPPGNAEVTTNIPKMEAATNQDQDGRTTNDISFGTSAVTPDIPLRATYPRTD 119
LRRC8C_Homo QPAQNHSSLSNVSQAVAS----------TTPLPPP-----K-- 85
LRRC8E_Homo LQENL-------SEA-PC----------QQLLPRG-----I-- 77
LRRC8B_Homo EFDNHCAVPWDILKA-SM----------NTSSNP--------- 83
E1H
TM2
LRRC8A_Homo ----STILPTPDTGPTGIKYDLDRHQYNYVDAVCYENRLHWFAKYFPYLVLLHTLIFLAC 139
LRRC8A_Mus ----STVLPTPDTGPTGIKYDLDRHQYNYVDAVCYENRLHWFAKYFPYLVLLHTLIFLAC 139
LRRC8A_Gallus ----SSLVPSPDTGPTGIQYDLDRHQYNYVDAVCYENRLHWFAKYFPYLVLLHTLIFLAC 139
LRRC8A_Xenopus ----STLSPPLAPGPTGIKYDLDRHQYNYVDAVCYENRLHWFAKYFPYLVLLHTLIFLAC 138
LRRC8D_Homo FALPNQEAKKEKKDPTGRKTNLDFQQYVFINQMCYHLALPWYSKYFPYLALIHTIILMVS 179
LRRC8C_Homo ----PSPANPITVEMKGLKTDLDLQQYSFINQMCYERALHWYAKYFPYLVLIHTLVFMLC 141
LRRC8E_Homo ----P-EQIGALQEVKGLKNNLDLQQYSFINQLCYETALHWYAKYFPYLVVIHTLIFMVC 132
LRRC8B_Homo --------GTPLPLPLRIQNDLHRQQYSYIDAVCYEKQLHWFAKFFPYLVLLHTLIFAAC 135
TM2
IL1H1
LRRC8A_Homo SNFWFKFPRTSSKLEHFVSILLKCFDSPWTTRALSETVVEESDPKPAFSKMN-GSMDKKS 198
LRRC8A_Mus SNFWFKFPRTSSKLEHFVSILLKCFDSPWTTRALSETVVEESDPKPAFSKMN-GSMDKKS 198
LRRC8A_Gallus SNFWFKFPRTSSKLEHFVSILLKCFDSPWTTRALSETVVEESDTKPAFGKMN-GSMDKKS 198
LRRC8A_Xenopus SNFWFKFPRTSSKLEHFVSILLKCFDSPWTTRALSETVVEESDPKPTGGKMN-GSVDKKS 197
LRRC8D_Homo SNFWFKYPKTCSKVEHFVSILGKCFESPWTTKALSETACEDSEENKQRITGAQTLP-KHV 238
LRRC8C_Homo SNFWFKFPGSSSKIEHFISILGKCFDSPWTTRALSEVSGEDSEEKDNRKNNMNRSNTI-Q 200
LRRC8E_Homo TSFWFKFPGTSSKIEHFISILGKCFDSPWTTRALSEVSGENQKGPAATERAAATIVAMAG 192
LRRC8B_Homo SNFWLHYPSTSSRLEHFVAILHKCFDSPWTTRALSETVAEQSVRPLKLSKSK-IL--LSS 192
IL1H2
LRRC8A_Homo STVSEDV--EAT--VPMLQRTKSRIEQGIVDRSETGVLDKKEGEQAKALFEKVKKFRTHV 254
LRRC8A_Mus STVSEDV--EAT--VPMLQRTKSRIEQGIVDRSETGVLDKKEGEQAKALFEKVKKFRTHV 254
LRRC8A_Gallus STVSEDV--EAT--VPMLQRTKSRIEQGIVDRSETGVLDKKEGEQAKALFEKVKKFRTHV 254
LRRC8A_Xenopus STASEDV--EAT--VPMLQRSKSRVEQGIVDRSETGVLDKKEGEQAKALFEKVKKFRTHV 253
LRRC8D_Homo STSSDEGSPSASTPMINKTGFKFSAEKPVIEVPSMTILDKKDGEQAKALFEKVRKFRAHV 298
LRRC8C_Homo SGP---E--GS---LVNSQSLKSIPEKFVVDKSTAGALDKKEGEQAKALFEKVKKFRLHV 252
LRRC8E_Homo TGP---G--KAG--EGEKEKVLAEPEKVVTEPPVVTLLDKKEGEQAKALFEKVKKFRMHV 245
LRRC8B_Homo SGCSADI--DSG--KQSLPYPQPGLESAGIESPTSSVLDKKEGEQAKAIFEKVKRFRMHV 248
TM3
E2β1
E2β2
LRRC8A_Homo EEGDIVYRLYMRQTIIKVIKFILIICYTVYYVHNIKFDVDCTVDIESLTGYRTYRCAHPL 314
LRRC8A_Mus EEGDIVYRLYMRQTIIKVIKFVLIICYTVYYVHNIKFDVDCTVDIESLTGYRTYRCAHPL 314
LRRC8A_Gallus EEGDIVYRLYMRQTIIKVIKFILIICYTVYYVNNITFDVDCKVDIESLTGYRMYRCAHPL 314
LRRC8A_Xenopus EEGDIVYRLYMRQTIIKVIKFIIILCYTVYYVSSIKFDVDCKVDIESLTGYRMYRCAHPL 313
LRRC8D_Homo EDSDLIYKLYVVQTVIKTAKFIFILCYTANFVNAISFEHVCKPKVEHLIGYEVFECTHNM 358
LRRC8C_Homo EEGDILYAMYVRQTVLKVIKFLIIIAYNSALVSKVQFTVDCNVDIQDMTGYKNFSCNHTM 312
LRRC8E_Homo EEGDILYTMYIRQTVLKVCKFLAILVYNLVYVEKISFLVACRVETSEVTGYASFCCNHTK 305
LRRC8B_Homo EQKDIIYRVYLKQIIVKVILFVLIITYVPYFLTHITLEIDCSVDVQAFTGYKRYQCVYSL 308
TM4
IL2H1
LRRC8A_Homo ATLFKILASFYISLVIFYGLICMYTLWWMLRRSLKKYSFESIREESSYSDIPDVKNDFAF 374
LRRC8A_Mus ATLFKILASFYISLVIFYGLICMYTLWWMLRRSLKKYSFESIREESSYSDIPDVKNDFAF 374
LRRC8A_Gallus ATLFKILASFYISLVVVYGLICMYTLWWMLRRSLKKYSFESIREESSYSDIPDVKNDFAF 374
LRRC8A_Xenopus ATLFKILASFYISLVGFYGLVCVYTLWWMLRRSLKKYSFESIREESSYSDIPDVKNDFAF 373
LRRC8D_Homo AYMLKKLLISYISIICVYGFICLYTLFWLFRIPLKEYSFEKVREESSFSDIPDVKNDFAF 418
LRRC8C_Homo AHLFSKLSFCYLCFVSIYGLTCLYTLYWLFYRSLREYSFEYVRQETGIDDIPDVKNDFAF 372
LRRC8E_Homo AHLFSKLAFCYISFVCIYGLTCIYTLYWLFHRPLKEYSFRSVREETGMGDIPDVKNDFAF 365
LRRC8B_Homo AEIFKVLASFYVILVILYGLTSSYSLWWMLRSSLKQYSFEALREKSNYSDIPDVKNDFAF 368
IL2H2
IL2H3
IL2H4
LRRC8A_Homo MLHLIDQYDPLYSKRFAVFLSEVSENKLRQLNLNNEWTLDKLRQRLTKNAQDKLELHLFM 434
LRRC8A_Mus MLHLIDQYDPLYSKRFAVFLSEVSENKLRQLNLNNEWTLDKLRQRLTKNAQDKLELHLFM 434
LRRC8A_Gallus MLHLIDQYDPLYSKRFAVFLSEVSENKLRQLNLNNEWTLEKLRQRITKNSQDKLELHLFM 434
LRRC8A_Xenopus MLHLIDQYDPLYSKRFAVFLSEVSENKLRQLNLNHEWTLDKLRQRITKNSQEKLELHLFM 433
LRRC8D_Homo LLHMVDQYDQLYSKRFGVFLSEVSENKLREISLNHEWTFEKLRQHISRNAQDKQELHLFM 478
LRRC8C_Homo MLHMIDQYDPLYSKRFAVFLSEVSENKLKQLNLNNEWTPDKLRQKLQTNAHNRLELPLIM 432
LRRC8E_Homo MLHLIDQYDSLYSKRFAVFLSEVSESRLKQLNLNHEWTPEKLRQKLQRNAAGRLELALCM 425
LRRC8B_Homo ILHLADQYDPLYSKRFSIFLSEVSENKLKQINLNNEWTVEKLKSKLVKNAQDKIELHLFM 428
LRRC8A_Danio MLHMIDQYDPLYSKRFAVFLSEVSENKLRQLNLNNEWTLEKLRQRITKNSQEKLELHLFM 420

Figure S1. Amino-acid sequence alignment of pore domains of LRRC8A orthologs and human LRRC8 paralogs, related to Figures 1–3.

The residues M1–M434 of the pore domain of HsLRRC8A are aligned with the equivalent residues of other orthologs and human LRRC8 paralogs. Residues of NT and TMs that are involved in polar interactions are highlighted in yellow. Secondary structures are marked for HsLRRC8A.

Figure S2

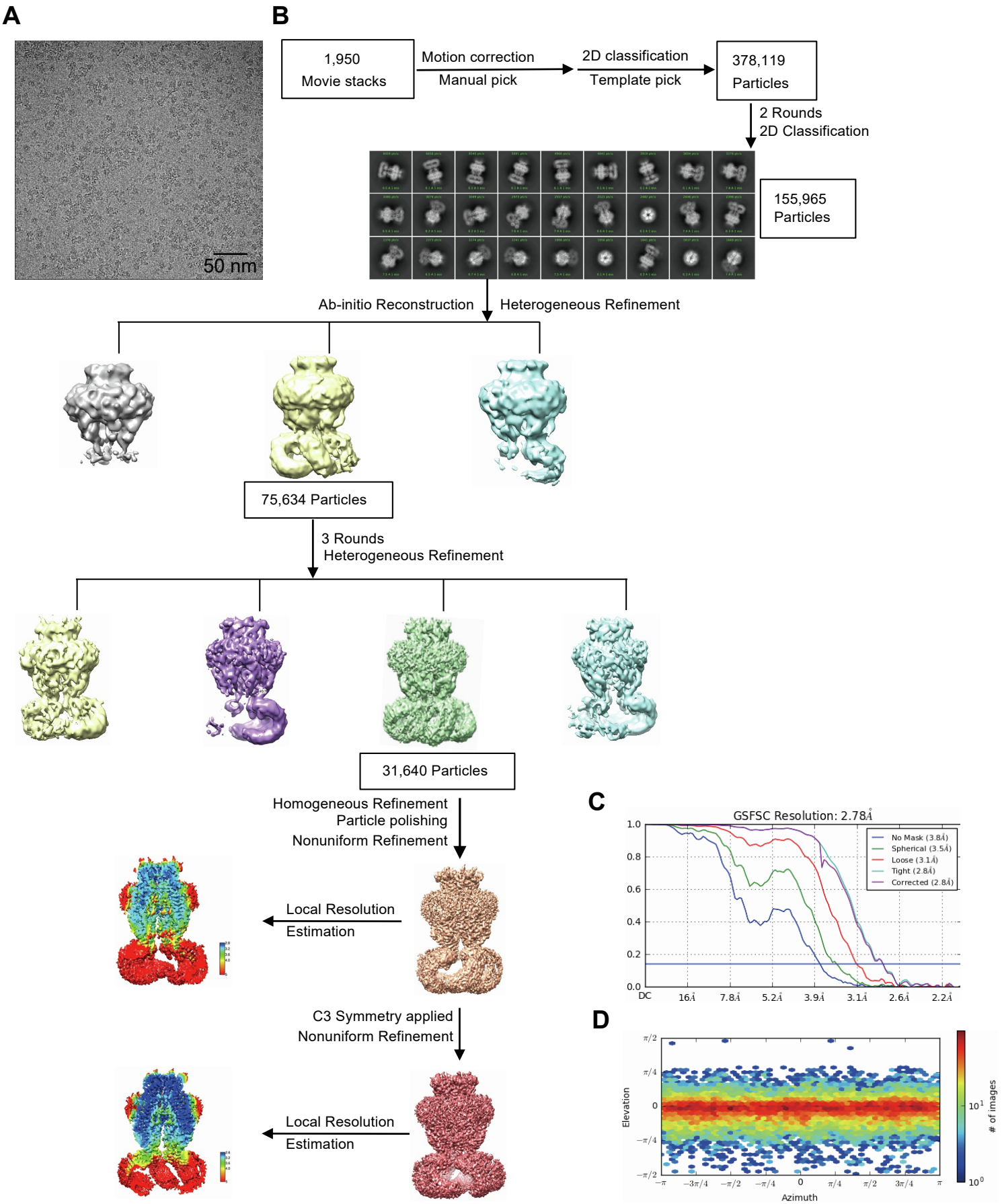

Figure S2. Reconstruction of cryo-EM structure of HsLRRC8A, related to Figures 1 and 2, and Table S1.

(A) Representative cryo-EM micrograph of dataset obtained at FEI Titan Krios. (B) Flowchart of HsLRRC8A reconstruction. Local resolution estimation is shown at the bottom panel. Flowchart of cryo-EM data processing of the HsLRRC8A structure, including particle picking, classification, and 3D refinement. (C) Fourier shell correlation (FSC) of the final 3D reconstruction following gold standard refinement. FSC curves are plotted before and after masking. (D) Angular distribution heatmap of particles used for the refinement.

Figure S3

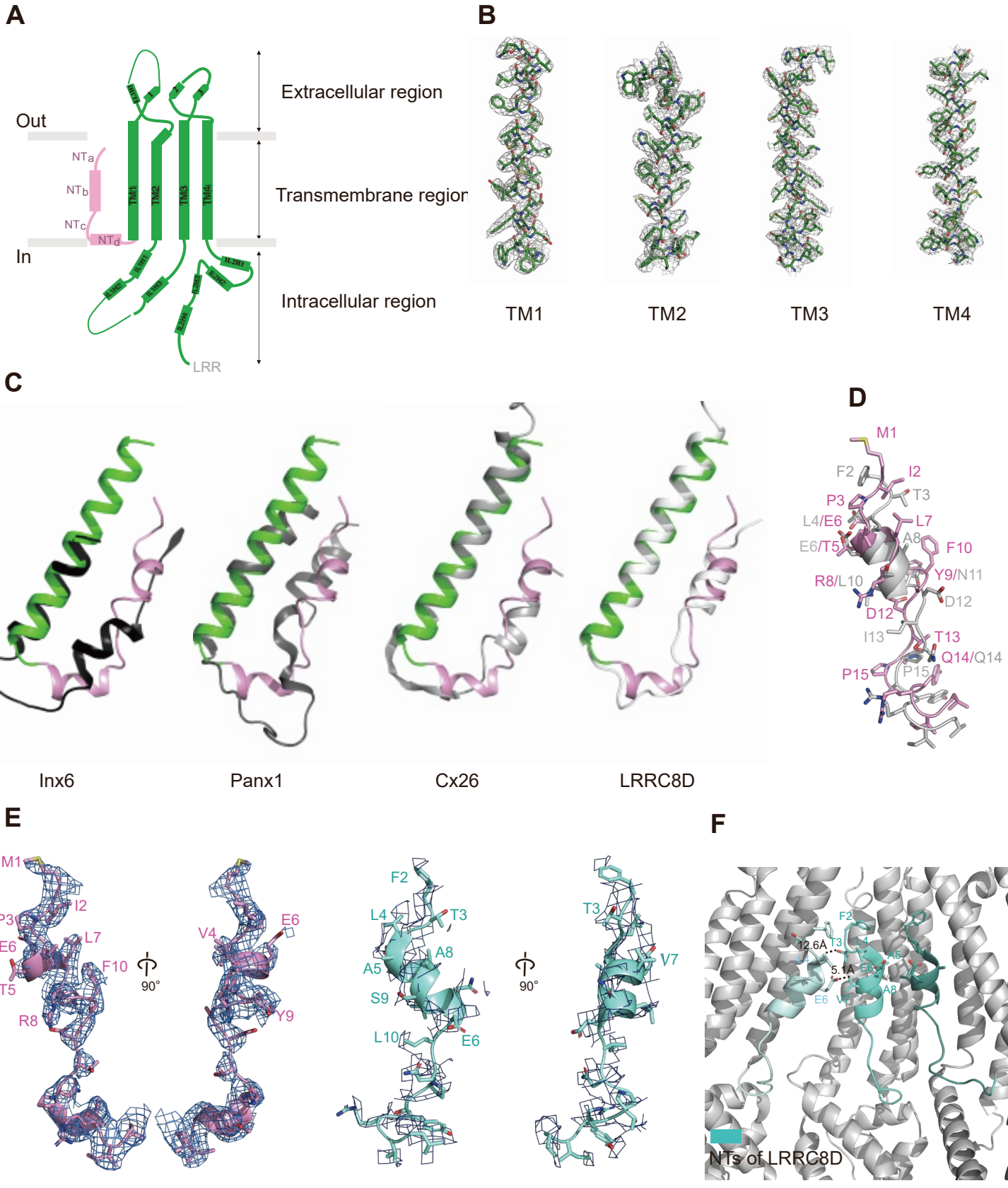

Figure S3. Subunit structure of HsLRRC8A, related to Figures 1 and 2.

(A) Schematic representation of the HsLRRC8A topology for the pore domain. (B) Cryo-EM density map (gray) for TMs. (C) Superimposition between HsLRRC8A NT and those of other large pore channels. PDB codes used in superimposition: INX6, 5H1Q[34]; Pannexin1, 6WBF[35]; Cx26, 2ZW3[33]; LRRC8D, 6M04[15]. (D) Superimposition of the HsLRRC8A NT (colored pink) and HsLRRC8D NT (colored grey), using the Cα atoms of the protomers. (E) Cryo-EM densities (contour level of each map is 2.0 σ) of NTs from a HsLRRC8A protomer (left) and a HsLRRC8D protomer (right), viewed from same orientations. (F) HsLRRC8D NTs and their local surroundings. No evident nonpolar and polar interactions were found between adjacent NTs.

Figure S4.

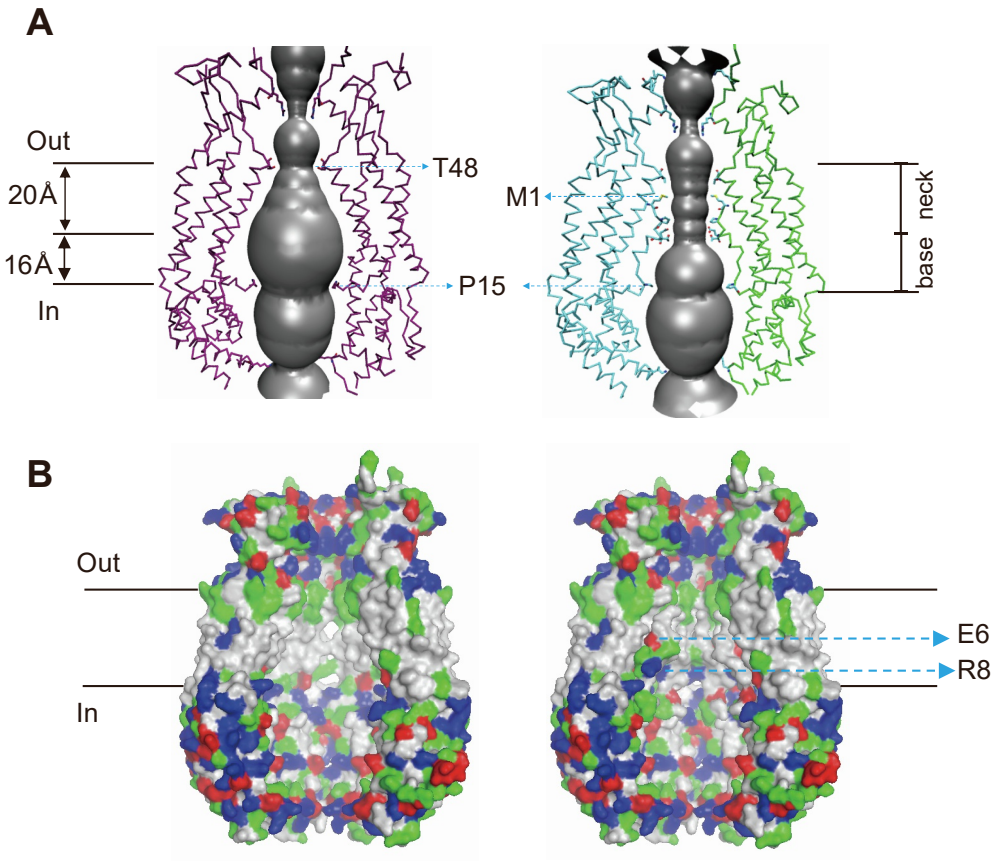

Figure S4. Permeation paths of LRRC8A channels containing unresolved NTs (left) and resolved NTs (right), related to Figures 1 and 2.

(A) Permeation paths relative to two opposite subunits. The neck and base have been marked. (B) Molecular surface of the permeation path viewed from the membrane. The surface is colored according to chemical properties of residues (hydrophobic, gray; hydrophilic, green; acidic, red; basic, blue). The PDB code is 5ZSU for HsLRRC8A containing the unsolved NTs. The two front subunits are removed for clarity.

Figure S5

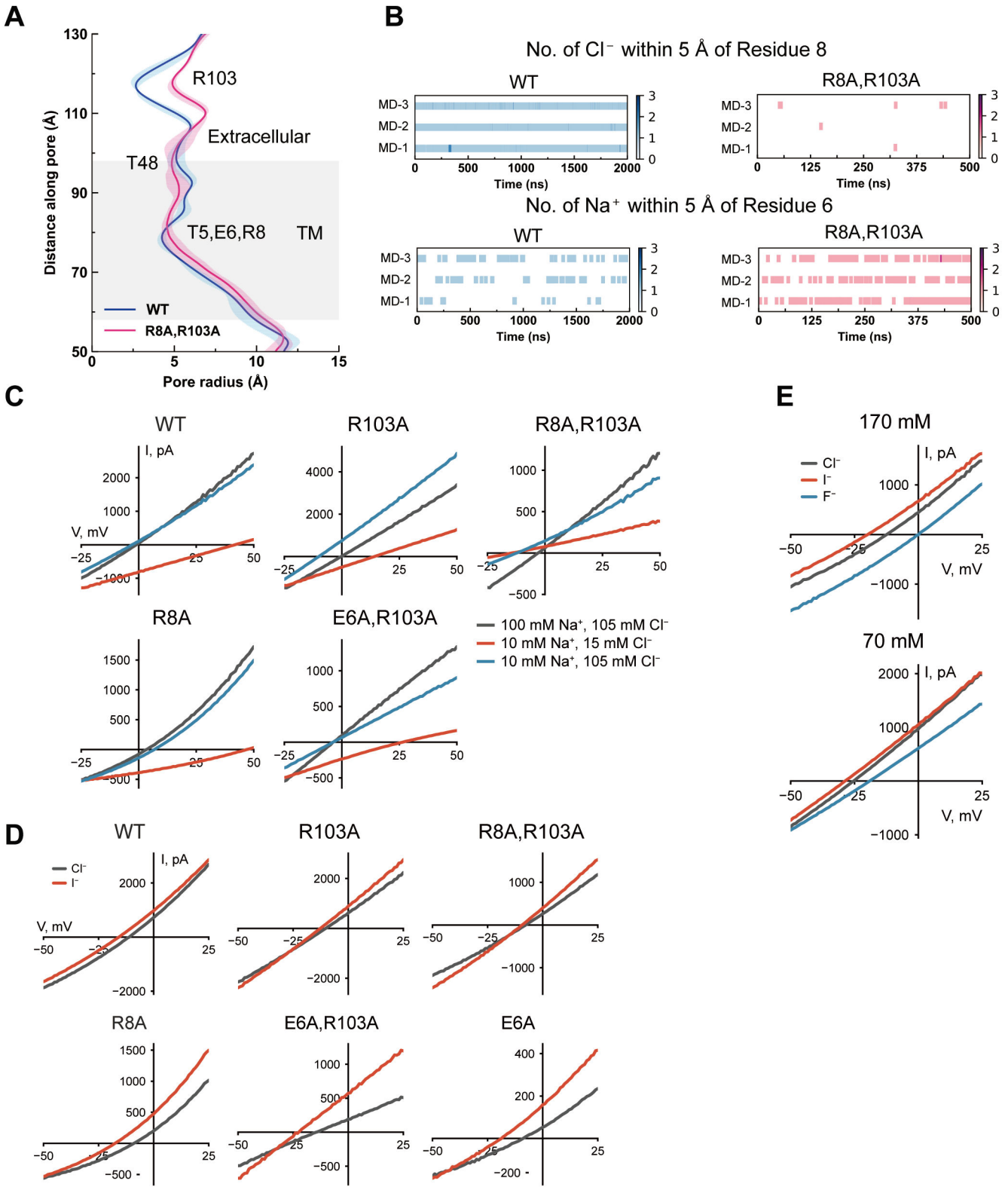

Figure S5. Influence of mutations on pore properties of LRRC8A channel as predicted by MD simulations (A and B) and tested by electrophysiology (C-E), related to Figure 3.

(A) Pore radius along the symmetry axis in WT (blue) and mutant (magenta) channels, respectively. The transmembrane segment of the pore domain is colored in grey. Radii were calculated from snapshots at 1-ns intervals in the last 1000-ns simulations. Data are shown as mean ± s.d. of three independent simulations for each system. (B) Number of Cl^- near residue 8 (top) and number of Na^+ near residue 6 (bottom) in WT (left) and the denoted mutant (right) channels during the course of simulations. (C) Averaged current traces from the recordings shown in Figures 3I and 3J, demonstrating the shifts in reversal potential between the high NaCl bath solution (gray), the low NaCl bath solution (red), and the low Na^+ (blue) bath solution. (D) Averaged current traces from the recordings shown in Figures 3K, 3L, and 3M, demonstrating the shifts in reversal potential between the NaCl (gray) and NaI (red) bath solutions. (E) Averaged current traces from the recordings shown in 4M and 4N, demonstrating the shifts in reversal potential between the NaCl- (gray), NaI- (red), and NaF-containing (blue) bath solutions.

Figure S6

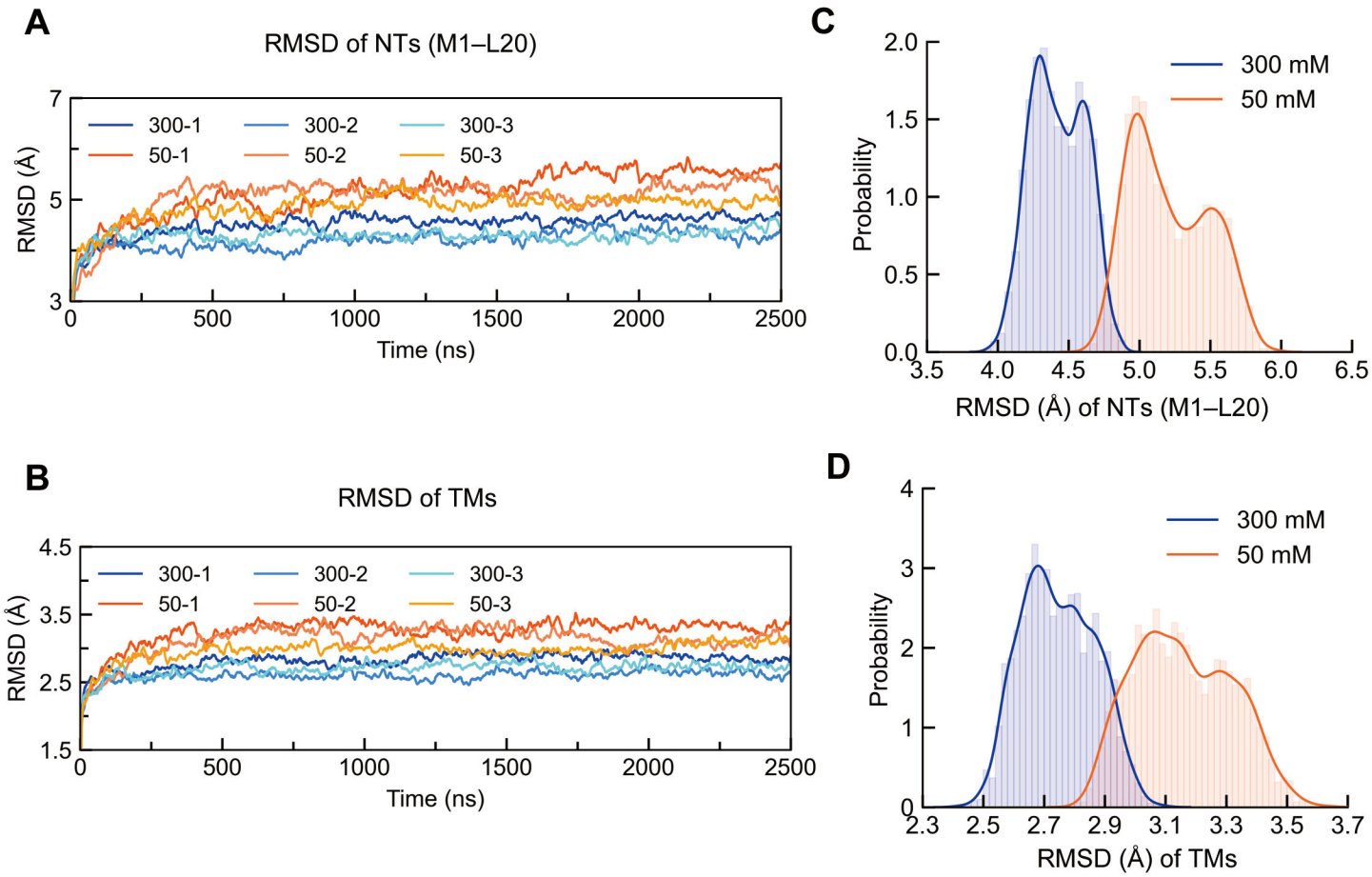

Figure S6. 2500-ns MD trajectories of RMSD values for residues of pore domain and their probability distributions generated from the last 1000-ns simulations, related to Figure 4.

The residue ranges of TMs were defined as: TM1, W23–T48; TM2, W120–K145; TM3, I259–N288; TM4, L314–M343. RMSD values of residues were calculated from their mainchain atoms sampled from snapshots at 100-ps intervals. (A and B) Trajectories of RMSD values for residues of NTs (A) or of TMs (B) in 2500-ns trajectories simulated at salt concentrations of 300 mM and 50 mM NaCl, respectively. Three independent simulations were performed at each salt concentration. (C and D) Probability distributions of RMSD values for residues of NTs (C) or of TMs (D) generated from the last 1000-ns trajectories.

Figure S7

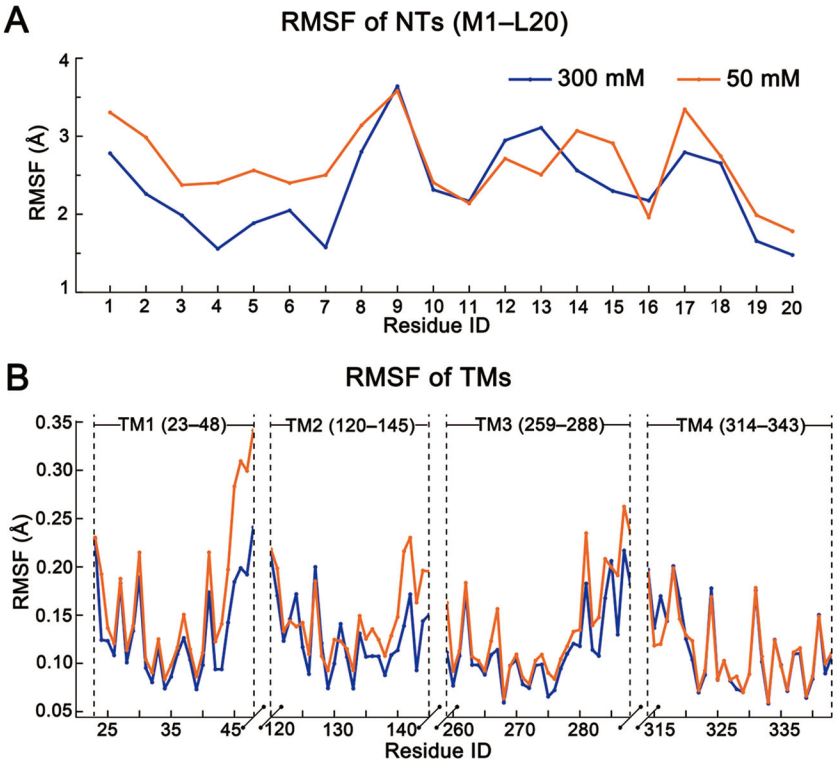

Figure S7. Root mean square fluctuations (RMSF) of each residue of NTs and TMs at 300 mM and 50 mM NaCl, related to Figure 4.

Root mean square fluctuations (RMSF) of each residue of NTs (A) and TMs (B) at 300 mM and 50 mM NaCl. Each subunit in a hexameric HsLRRC8A channel was treated equally. The RMSF value of each residue was calculated based on 18,000 sampled snapshots from all three parallel simulations, as the last 1000-ns snapshots at 1-ns intervals for each of the six subunits were used.

Figure S8

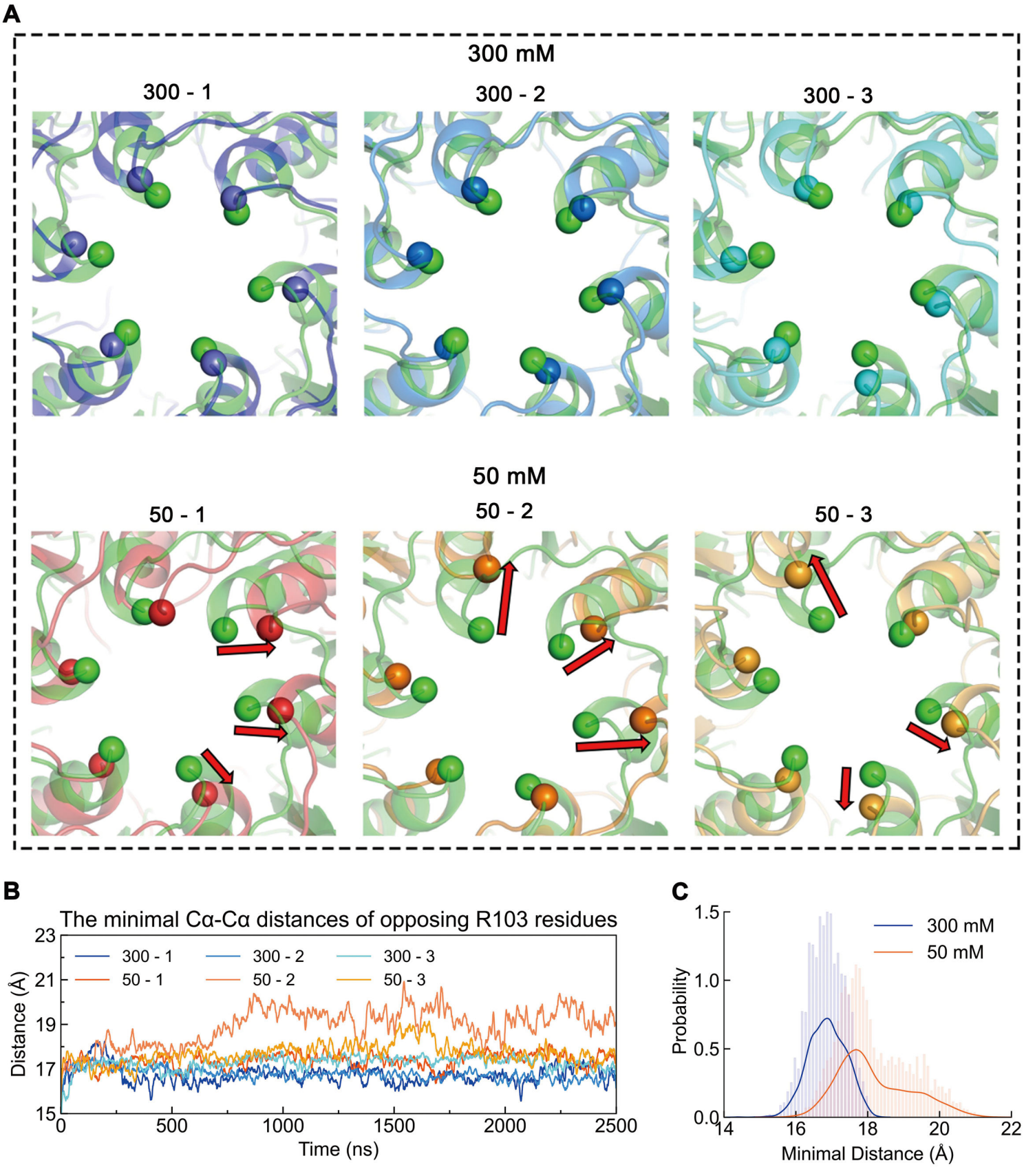

Figure S8. Radial movements of R103 in MD simulations conducted at 300 mM and 50 mM NaCl concentrations, related to Figure 4.

(A) Superposition of representative structures obtained at each salt concentration with the cryo-EM structure (colored in green) of HsLRRC8A, viewed from the top. Cα atoms of R103 residues were depicted as spheres. The red arrows indicate the radial dilation of Cα atoms of R103 residues at 50 mM NaCl. (B) The time evolution of minimal Cα-Cα distances between opposing R103 residues. (C) The probabilities of the Cα-Cα minimal distances calculated for the last 1000-ns simulations.

Figure S9

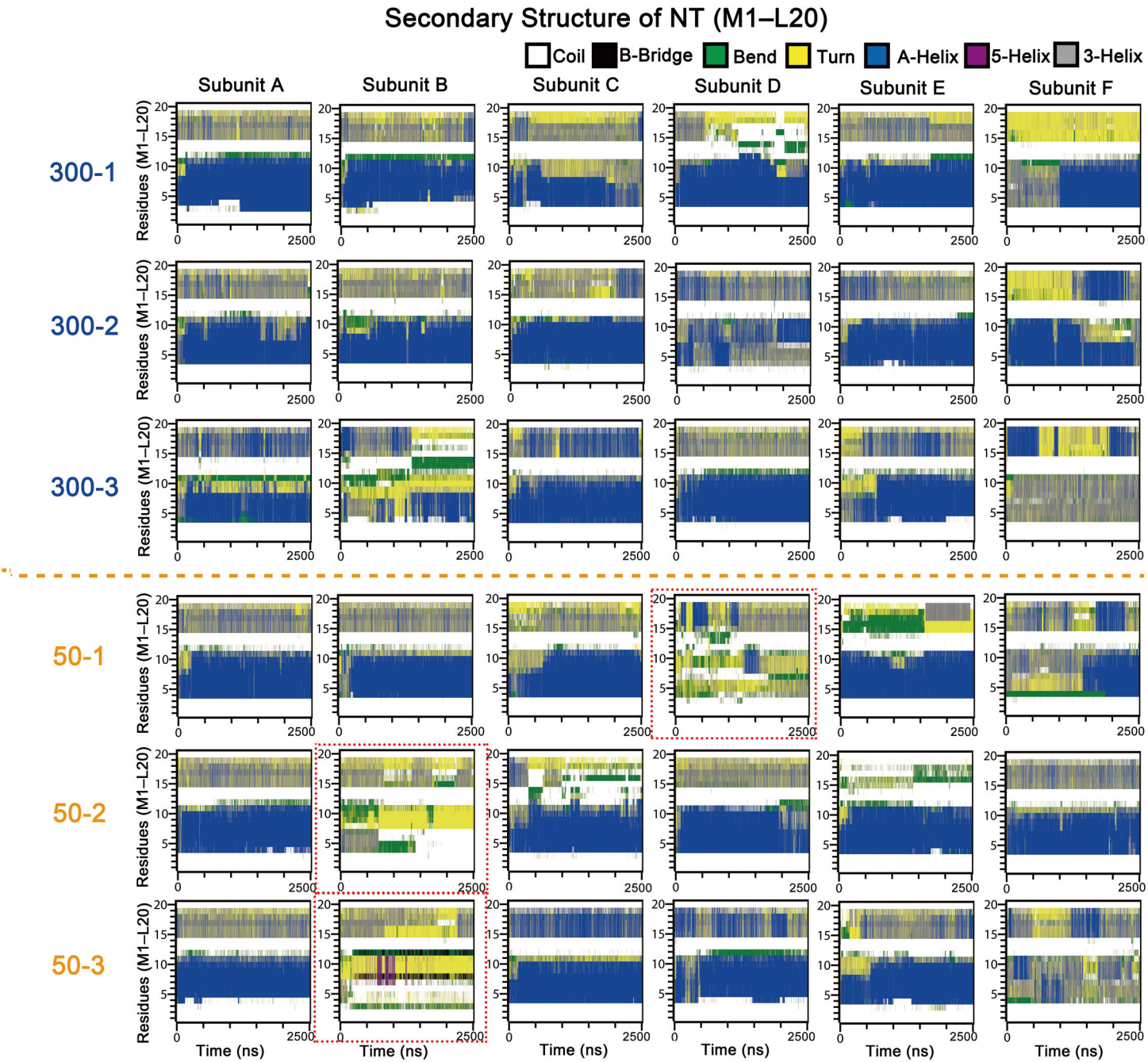

Figure S9. The changes in secondary structures of NT subsegments during the course of simulations, related to Figure 4.

The unwound subsegments at 50 mM NaCl are highlighted by red dashed boxes.

Table S1. Cryo-EM data collection, refinement, and validation statistics, related to Figure 1 and Figure S2.

Data collection and processing	
Microscope	FEI Titan Krios
Camera	K3
Voltage (kV)	300kV
Magnification	105K
Pixel size (Å)	0.52 (1.04)
Electron exposure (e–/Å^2)	~60
Defocus range (μm)	–1.0 to –2.2
Symmetry imposed	C3
Initial particle images (no.)	378,119
Final particle images (no.)	31,640
Map resolution (Å)	2.78
FSC threshold	0.143
Refinement	
Initial model used (PDB code)	6G9O
d model	3.2
dFSC model (0/0.143/0.5)	2.7/2.8/3.2
Map sharpening B factor (Å^2)	–78
Model composition	
Non-hydrogen atoms	36203
Protein residues	4385
B factor (Å^2)	304.66
R.m.s. deviations	
Bond lengths (Å)	0.009
Bond angles (°)	1.267
Validation	
MolProbity score	1.92
Clash Score	10.34
Poor rotamers (%)	0
Ramachandran plot	
Favored (%)	95.37
Allowed (%)	4.47
Disallowed (%)	0.16

Table S2. Cα-Cα distance between pairs of opposite residues that constitute the constriction sites along the permeation path, related to Figures 1 and 2.

Distance (Å) between Cα atoms of opposite residues	R103	T48	M1 / P3	E6	P15	K235
HsLRRC8A	14.7	16.8	22.7 / 17.1	19.9	28.5	24.5
6G9O	15.7	16.9	NA	NA	27.5	28.2
6NZW	15.5	18.3	NA	NA	28.7	27.7
6NZZ	16.1	18.3	NA	NA	32.4	31.9
5ZSU	16.2	18.4	NA	NA	NA	33.9
6DJB	15.3	18.8	NA	NA	35.5	31.0

Table S3. Buried surface area in the interface between two adjacent subunits of the pore domain, related to Figure 2. The extracellular, transmembrane and intracellular portions of pore domain are same as those in Figure 1.

Buried surface (Å^2)	HsLRRC8A	6G9O	5ZSU (loose/tight interface)	6DJB	6NZW	6NZZ
Total	2180	1683	1701/1051	1668	1590	1537
Extracellular segment	920	915	850/805	860	887	920
Transmembrane segment	810	380	376/234	302	379	314
Contribution of N-halves to transmembrane segment	770	NA	NA	NA	NA	NA
Contribution of C-halves to transmenbrane segment	445	NA	NA	NA	NA	NA
Intracellular segment	490	328	464/NA	398	311	266